processes

MDPI

Article

Zr-MOF Crosslinked Hydrogel for High-Efficiency Decontamination of Chemical Warfare Agent Simulant

Saijie Li [1,2], Lei Wang [2], Jiayi Zhang [2], Yun Liang [1], Min Tang [1], Guilong Xu [1,*] and Chunyu Wang [2,*]

[1] School of Light Industry and Engineering, South China University of Technology, Guangzhou 510640, China; 202221029431@mail.scut.edu.cn (S.L.); liangyun@scut.edu.cn (Y.L.); tangmin88@scut.edu.cn (M.T.)
[2] State Key Laboratory of NBC Protection for Civilian, Beijing 100191, China; alvin-leilei@126.com (L.W.); woyaohaochide@163.com (J.Z.)
* Correspondence: feglxu@scut.edu.cn (G.X.); wcy18@tsinghua.org.cn (C.W.)

Abstract: The decontamination of chemical warfare agents (CWAs) from contaminated surfaces is of critical importance due to the severe threats posed by CWAs to human health and the environment, particularly given the persistent threat of chemical weapons since World War I. In this study, a novel UiO-66-NH_2 crosslinked hyaluronic acid (HA) hydrogel was developed in the presence of polyvinyl alcohol under ambient conditions, leveraging the dual functionality of the amino-substituted zirconium-based metal–organic framework (Zr-MOF) as both a crosslinker and a catalytic site. The hydrogel demonstrated exceptional catalytic performance, achieving a degradation efficiency of over 90% for the chemical warfare agent simulant dimethyl 4-nitrophenyl phosphate (DMNP) within 1 h. Furthermore, the hydrogel demonstrated adequate mechanical and tensile strength for practical use, enabling easy peel-off from various contaminated surfaces without leaving residues. This peelable property, combined with its decontamination capabilities, highlights its significant potential for practical applications in the field of CWA decontamination.

Keywords: MOF crosslinked hydrogel; catalytic decontamination; chemical warfare agent simulant degradation; peelable

check for updates

Academic Editor: Christos Argirusis

Received: 28 February 2025
Revised: 19 March 2025
Accepted: 21 March 2025
Published: 25 March 2025

Citation: Li, S.; Wang, L.; Zhang, J.; Liang, Y.; Tang, M.; Xu, G.; Wang, C. Zr-MOF Crosslinked Hydrogel for High-Efficiency Decontamination of Chemical Warfare Agent Simulant. *Processes* **2025**, *13*, 973. https://doi.org/10.3390/pr13040973

Copyright: © 2025 by the authors. Licensee MDPI, Basel, Switzerland. This article is an open access article distributed under the terms and conditions of the Creative Commons Attribution (CC BY) license (https://creativecommons.org/licenses/by/4.0/).

1. Introduction

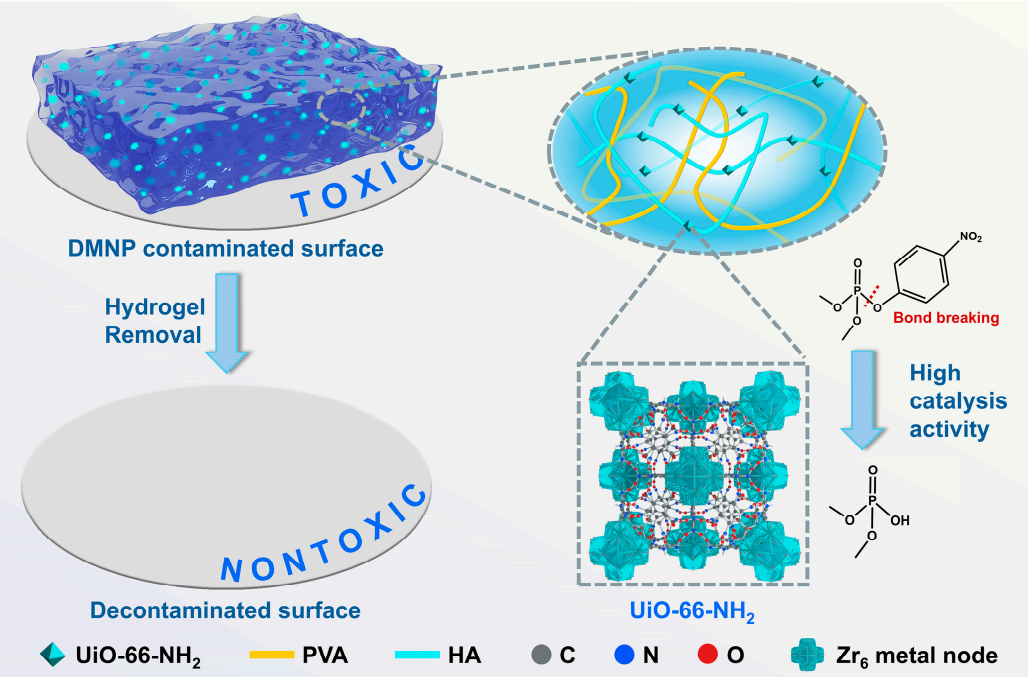
Chemical warfare agents (CWAs) [1], particularly nerve agents such as Sarin (GB), Soman (GD), and VX, continue to pose a significant threat to both military and civilian security [2,3]. Nerve agents, which typically contain phosphate ester bonds, readily bind to acetylcholinesterase (AChE), a critical enzyme in the central nervous system [4]. This binding inhibits AChE activity, leading to the accumulation of acetylcholine and subsequent overstimulation of the nervous system. Such effects can result in respiratory failure and death within minutes [3,5]. Due to their high toxicity, rapid action, and environmental persistence, there is an urgent need to develop efficient decontamination methods that can rapidly and safely neutralize these agents.

Current approaches to degrading nerve agents primarily rely on materials such as enzymes [6], metal oxides [7,8], organic polymers [9,10], and polyoxometalates [11]. However, these systems often suffer from limitations such as slow reaction kinetics and the deactivation of active sites, which hinder their effectiveness in CWA degradation [12,13]. In contrast, metal–organic frameworks (MOFs) have emerged as a promising class of porous materials with unique advantages for the detoxification of CWA simulants [14–16]. MOFs exhibit large surface areas, high porosity, well-defined pore structures, ordered frameworks, and tunable functionality [17]. Notably, Zr-MOFs featuring exposed bimetallic

Zr-OH-Zr active sites, such as UiO-66, NU-1000, and MOF-808, have demonstrated efficient catalytic hydrolysis of organophosphate nerve agents and simulants in alkaline aqueous solutions [18,19]. Despite their promising performance, the practical application of MOFs in CWA degradation faces challenges related to the immobilization and recovery of powdered materials, as well as long-term stability [20]. To address these issues, researchers have explored the integration of MOFs into mechanically robust, high-water-content, and flexible polymer-based hydrogels.

For example, Farha et al. designed Zr-MOF/hydrogel fiber composites for the degradation of organophosphate compounds, investigating the influence of Zr-node connectivity, linker functionality, and topology on degradation efficiency [21]. Yang et al. developed a super-alkaline microreactor capable of spontaneous moisture absorption, which integrated Zr-MOF catalysts with alkaline poly (dimethylaminoethyl acrylate) through photo-induced polymerization on lithium chloride (LiCl)-salted poly (N-isopropylacrylamide) gels [22]. This system demonstrated effective detoxification of DMNP in atmospheric conditions. While hydrogels have demonstrated significant advantages in CWA decontamination, the potential of MOF-based hydrogels in this field remains largely unexplored. Rotariu et al. developed photo-crosslinked interpenetrating network hydrogels capable of trapping toxic substances within the hydrogel matrix during decontamination [23]. Chen et al. designed a poly (vinyl alcohol) (PVA)/Borax/$NaBO_3$ sprayable hydrogel that exhibited excellent decontamination performance on porous and vertical surfaces, allowing for complete removal from the substrate after use [23]. Diacon et al. introduced ionically crosslinked hydrogels with photocatalytic properties, providing a green and effective method for decontaminating surfaces exposed to mustard gas (HD), with residues encapsulated within the hydrogel film [24]. Although MOF-based hydrogels show great potential for the degradation of chemical warfare agents, a system capable of stable existence in atmospheric environments while catalytically degrading CWAs on contaminated surfaces has yet to be developed.

Herein, we prepared a novel high-performance PVA/HA/U6N hydrogel as illustrated in Scheme 1. In this hydrogel, the amino-functionalized zirconium-based MOF (U6N) serves not only as an efficient hydrolysis catalyst for the rapid degradation of CWA simulants on contaminated surfaces but also enhances the mechanical strength of the hydrogel through crosslinking with hyaluronic acid (HA). The high-density Zr-OH-Zr active sites in U6N catalyze the hydrolysis of P-O bonds, producing low-toxicity 4-nitrophenol (4-NP) and dimethyl phosphate as byproducts. Upon completion of the catalytic degradation, the hydrogel achieves complete delamination from the contaminated substrate, enabling efficient surface purification. This innovative approach not only enhances the efficiency and scalability of decontamination processes but also provides a versatile, environmentally friendly, and user-friendly solution for mitigating the risks associated with chemical warfare agents.



Scheme 1. Illustration of PVA/HA/U6N MOF-based hydrogel for decontamination of polluted surfaces.

2. Experimental Section

2.1. Chemicals and Materials

The 2-Aminoterephthalic acid (NH_2-H_2BDC) and Zirconium chloride ($ZrCl_4$) were purchased from Shanghai Aladdin Biochemical Technology Co., Ltd. (Shanghai, China). Anhydrous ethanol, methanol and N,N-dimethylformamide (DMF) were obtained from Beijing InnoChem Science & Technology Co., Ltd. (Beijing, China). Acetic acid was supplied by Shanghai Maclin Biochemical Co., Ltd. (Shanghai, China). The 1-(3-Dimethylaminopropyl)-3-ethylcarbodiimide hydrochloride (EDC), N-hydroxysuccinimide (NHS), and hyaluronic acid (molecular weight: 800,000–1,500,000 Da) were purchased from Shanghai Aladdin Biochemical Technology Co., Ltd. PVA (alcoholysis degree: 87–89 mol/mol) was provided by Shanghai Maclin Biochemical Co., Ltd. DMNP was purchased from BIOFOUNT Co., Ltd. (Beijing, China). All chemicals were of analytical grade and used without further purification. Deionized water was used throughout all experimental procedures.

2.2. Synthesis of U6N

U6N was synthesized based on a typical solvothermal protocol modified slightly by changing the amount of raw materials [20]. $ZrCl_4$ (2.2 mmol) and 2-aminoterephthalic acid (2.4 mmol) were dissolved in 13 mL of DMF, followed by the addition of 17 mL acetic acid as a modulator. The solution was then transferred into a 50 mL Teflon-lined autoclave, and heated at 120 °C for 24 h. After cooling to room temperature, the resulting product was washed three times with DMF to remove unreacted precursors. To ensure complete removal of residual DMF, the product was further dispersed in methanol for 3 days. Finally, the synthesized U6N was washed with ethanol and dried under vacuum at 90 °C.

2.3. Formation of PVA/HA/U6N

A certain amount of hyaluronic acid (HA) and U6N were separately dispersed in deionized water, followed by the addition of excess EDC and NHS to each solution. The mixtures were then sonicated for 30 min. The two solutions were combined and thoroughly mixed, after which a specific amount of PVA solution was added. The mixture was stirred vigorously and allowed to stand, eventually forming a hydrogel. The hydrogels

were named based on the percentage composition of each component, designated as 4PVA2HA0.5U6N, 4PVA2HA1U6N, and 4PVA2HA2U6N, respectively.

2.4. Characterization

The chemical compositions and structures were characterized using a ZEISS GeminiSEM 300 scanning electron microscope (SEM), a Rigaku Ultima IV Advance X-ray diffractometer (XRD), a Thermo Fisher Scientific Nicolet iS20 Fourier-transform infrared (FT-IR) spectrometer, and a Thermo Scientific K-Alpha X-ray photoelectron spectroscope (XPS). The absorbance spectra were collected with a Shimadzu UV-3600 UV–visible (UV–vis) spectrophotometer. The rheological properties of the hydrogel were measured using a Haake Mars40 stress-controlled rheometer equipped with parallel plates (Φ = 25 mm, gap = 1 mm). The mechanical resistance of the hydrogels under uniaxial tensile deformation was evaluated using a UTM 6103 testing machine in strain ramp mode at a constant rate of 2 mm/min.

2.5. Catalytic Degradation of DMNP by U6N and PVA/HA/U6N

The catalytic degradation of DMNP was carried out according to the reports in previous literature [25]. First, 1 mL of N-ethylmorpholine solution (N-EM, 0.45 M, pH = 10) was added to four centrifuge tubes, each containing 0.0025 mmol of U6N. Hydrogels prepared with mass ratios of PVA:HA:U6N = 8:4:1, 4:2:1, and 2:1:1 (M_{U6N} = 0.0025 mmol) were added to three of the centrifuge tubes, respectively. The four tubes were then sonicated for 30 min to ensure thorough mixing and the formation of a homogeneous and stable dispersion. After sonication, the tubes were transferred to a magnetic stirrer. Subsequently, 4 μL of DMNP was added to each of the four tubes, and the solutions were maintained at a constant stirring speed to ensure complete mixing and efficient reaction progression. During the reaction, at predetermined time intervals (t = 2 min, 5 min, 10 min, 20 min, 30 min, 40 min, 60 min, and 120 min), 20 μL of the mixture was extracted from each tube and rapidly diluted with 10 mL of N-EM solution. The diluted solutions were then analyzed using a UV–Vis spectrophotometer. The catalytic efficiency was evaluated by monitoring the UV absorbance of the reaction product, 4-nitrophenol, at 404 nm.

2.6. Adhesive Properties and Peelability of the Hydrogel

To evaluate the adhesive properties of the hydrogel, the 4PVA2HA0.5U6N hydrogel was applied to both glass and plastic surfaces. Its adhesion capability on these materials was assessed through macroscopic observation. To investigate the peelability of the hydrogel, the same formulation was coated onto surfaces such as glass, wood, ceramic tiles, and stainless steel plates. The process of the hydrogel film being completely peeled off from each substrate was observed and recorded, providing insights into its practicality and suitability for practical deployment.

3. Results and Discussion

3.1. Characterization of U6N

U6N nanoparticles were successfully synthesized via a microwave-assisted solvothermal method (Figure 1a). To comprehensively characterize their structural properties, the surface morphology and particle size distribution of the product were analyzed using SEM (Figure 1b). The results revealed that the MOF particles exhibited a regular octahedral morphology with an average particle size of 700 nm, demonstrating excellent size uniformity. The XRD pattern (Figure 1c) showed that the synthesized material matched the simulated U6N, with characteristic diffraction peaks appearing at 2θ angles of 7.2°, 8.4°, 11.9°, 25.6°, and 32.9°, corresponding to the (111), (002), (022), (224), and (137) crystal planes,

respectively [26]. These characteristic peaks further confirmed that the crystal structure of U6N adopts a face-centered cubic configuration, indicating that the synthesized material possesses high crystallinity and structural integrity.

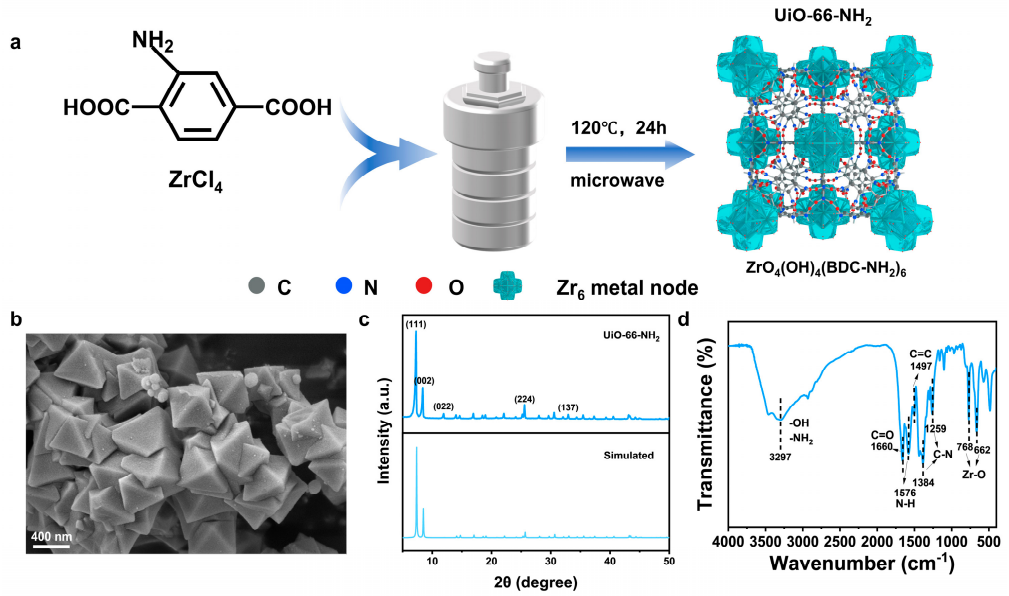


Figure 1. (**a**) Schematic illustration of the solvothermal synthesis of U6N, (**b**) SEM image of U6N, (**c**) XRD pattern of U6N and simulated U6N, and (**d**) FT−IR spectra of U6N.

To further verify the chemical structure of U6N, FT-IR was employed. In the FT-IR spectrum (Figure 1d), the broad absorption peak at 3297 cm^{-1} was attributed to the stretching vibrations of -NH_2 and -OH bonds [27]. The characteristic peaks at 1660 cm^{-1} and 1576 cm^{-1} corresponded to C=O and N-H, respectively, while the peak at 1497 cm^{-1} was assigned to the C=C bond in the benzene ring [28]. Additionally, the peaks at 1259 cm^{-1} and 1384 cm^{-1} were associated with the vibrational modes of C-N bonds between aromatic carbon and nitrogen [29]. Furthermore, the peaks observed at 768 cm^{-1} and 662 cm^{-1} were attributed to Zr-O bond vibrations [30], providing further evidence for the formation of metal–organic ligand bonds.

To elucidate the surface chemical composition of U6N, XPS analysis was systematically performed. As demonstrated in Figure 2a, the characteristic core-level spectra of N 1s, C 1s, and O 1s collectively confirm the successful integration of 2-aminoterephthalate ligands within the framework. The high-resolution Zr 3d spectrum (Figure 2b) exhibits two well-defined peaks at 185.1 eV (Zr $3d_{3/2}$) and 182.8 eV (Zr $3d_{5/2}$), characteristic of Zr coordinated with carboxylate groups, confirming the formation of stable Zr-O coordination bonds [31]. Deconvolution of the C 1s spectrum (Figure 2c) reveals three distinct components at 284.5 eV (C-C), 285.7 eV (C-N), and 288.5 eV (O-C=O) [32]. Furthermore, the O 1s spectrum (Figure 2d) was resolved into three contributions at 530.6 eV (Zr-O), 531.6 eV (-OH), and 532.8 eV (O=C-O), providing compelling evidence for the successful coordination between $ZrCl_4$ and NH_2-H_2BDC [33]. Collectively, these comprehensive characterization results conclusively demonstrate the successful synthesis of U6N and its structural integrity.

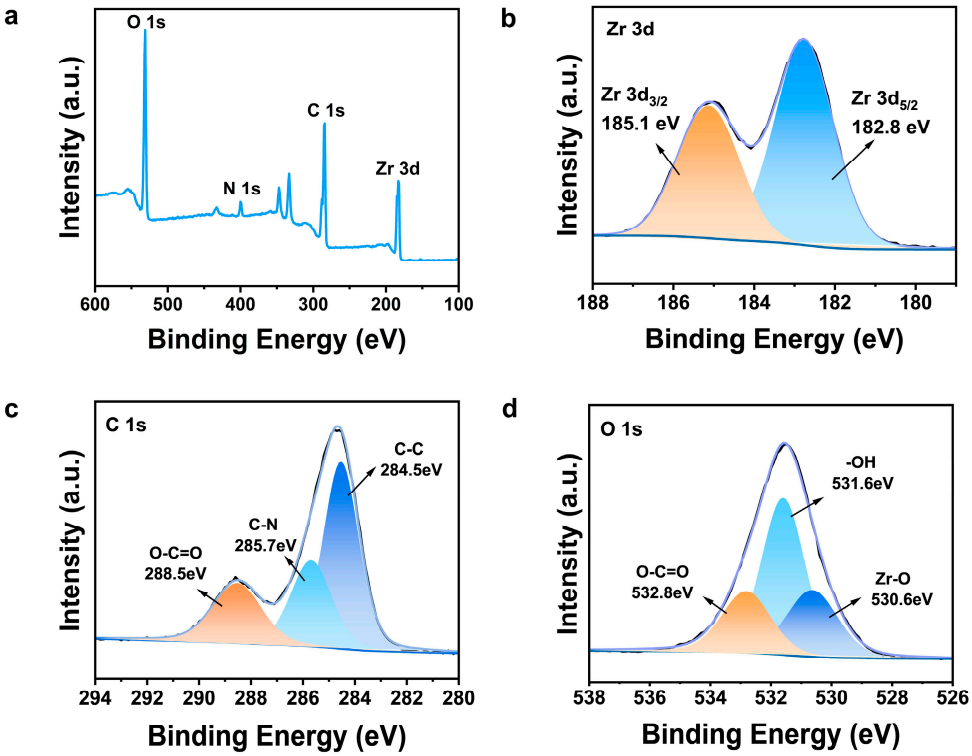


Figure 2. (**a**) XPS survey spectra of UiO-66-NH_2, high-resolution XPS spectra of (**b**) Zr 3d, (**c**) C 1s, and (**d**) O 1s of UiO-66-NH_2.

3.2. Characterization of PVA/HA/U6N Hydrogels

The covalent crosslinking between amino groups on U6N surfaces and carboxyl groups in HA was achieved via an EDC/NHS-mediated amidation reaction in the presence of PVA, which facilitated the assembly of a three-dimensional hierarchical network. (Figure 3). The 4PVA2HA1U6N hydrogel was selected for characterization experiments.

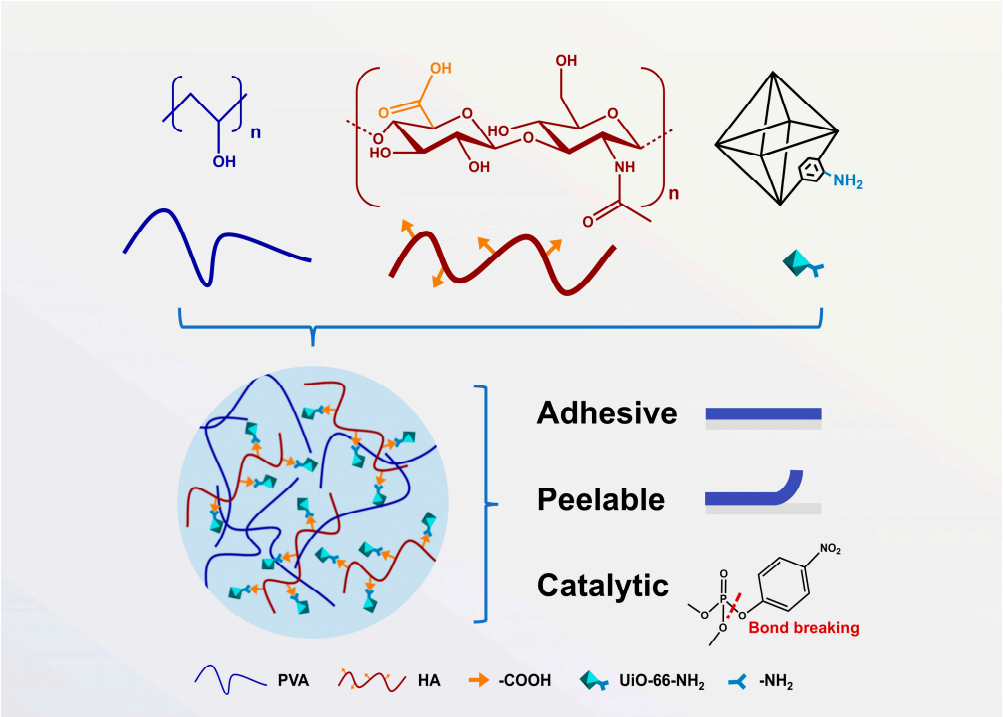


Figure 3. Schematic illustration of hydrogel (PVA/HA/U6N) synthesis and characterization.

Figure 4a illustrates the synthesis process of the 4PVA2HA1U6N hydrogel before and after formation. The gelation phenomenon was observed experimentally, and the successful synthesis of the hydrogel was confirmed using the vial inversion method. Upon mixing the components, a viscous fluid-like hydrogel formed, which transitioned into a solid hydrogel after a certain period. The as-prepared PVA/HA/U6N hydrogel exhibited a translucent and homogeneous appearance with a smooth surface morphology, demonstrating excellent structural uniformity and surface integrity. The cross-section of the freeze-dried hydrogel, fractured in liquid nitrogen, is shown in Figure 4b, revealing a porous three-dimensional crosslinked network structure with internal pore diameters ranging from 8 μm to 230 μm. FT-IR and XPS analyses were employed to characterize the composition and structure of the hydrogel.

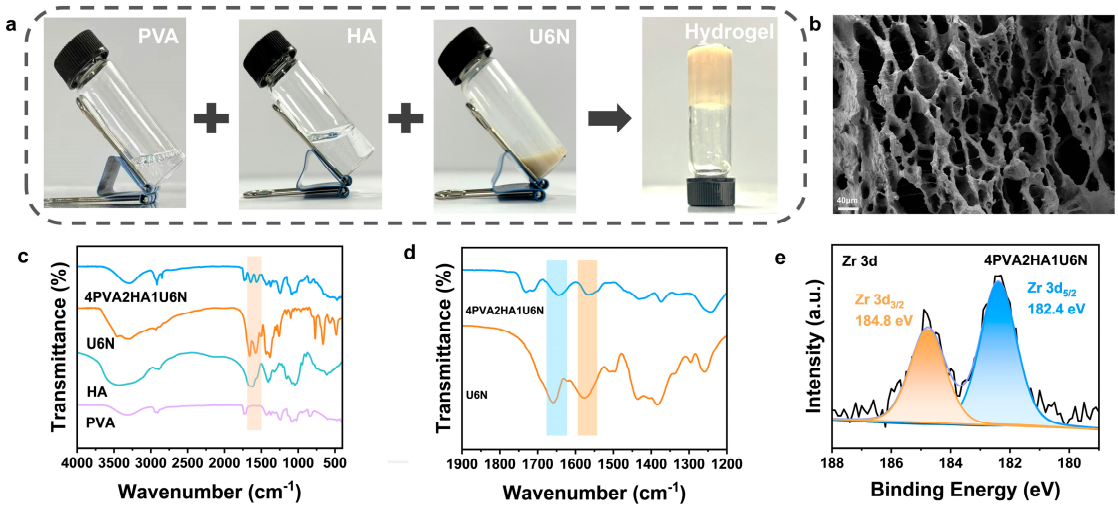


Figure 4. (**a**) Macroscopic observation of hydrogel formation, (**b**) SEM image of 4PVA2HA1U6N, (**c**) FT-IR spectra of 4PVA2HA1U6N, U6N, HA, and PVA, (**d**) magnified FT-IR spectrum in the range of 1200−1900 cm^{-1}, and (**e**) Zr 3d XPS spectra of 4PVA2HA1U6N hydrogel.

The FT-IR analysis (Figure 4c) displayed characteristic peaks of U6N at 1660 cm^{-1} and 1576 cm^{-1}, corresponding to C=O and N-H, respectively. The results in Figure 4d indicated that after hydrogel synthesis, the C=O peak shifted from 1660 cm^{-1} to around 1644 cm^{-1}, while the N-H peak shifted from 1576 cm^{-1} to approximately 1560 cm^{-1}, consistent with previous studies [11]. This shift suggests the formation of amide bonds between the amino groups on U6N and the carboxyl groups in HA. The XPS spectra (Figure 4d) showed minimal changes in the Zr 3d peaks between U6N and PVA/HA/U6N, indicating that the interaction between Zr and O in the ligands was only slightly affected during the synthesis process. This observation further confirms the high stability of the material. Furthermore, XPS analysis of the 4PVA2HA1U6N hydrogel revealed that its Zr 3d spectrum could be deconvoluted into two characteristic peaks, corresponding to Zr $3d_{5/2}$ (182.4 eV) and Zr $3d_{3/2}$ (184.8 eV), respectively. The Zr 3d binding energy of the 4PVA2HA1U6N hydrogel exhibited a negative shift compared to pristine U6N, with the characteristic peaks shifting from 182.8 eV (Zr $3d_{5/2}$) and 185.2 eV (Zr $3d_{3/2}$) in the parent material. Compared to the Zr 3d spectrum of pristine U6N (Zr $3d_{5/2}$ at 182.8 eV and Zr $3d_{3/2}$ at 185.2 eV), the Zr 3d binding energy of the 4PVA2HA1U6N hydrogel exhibited a negative shift. This observation suggests that an interaction occurs between hyaluronic acid (HA) and U6N in the 4PVA2HA1U6N hydrogel system, leading to an increase in the electron density around the Zr center and consequently a reduction in its binding energy.

XRD analysis was performed on hydrogels with varying U6N content to investigate their structural properties. As shown in Figure 5, the characteristic diffraction peaks of

U6N (2θ = 7.2°, 8.4°, 11.9°, 25.6°, and 32.9°) remained present in the PVA/HA/U6N hydrogels, indicating that the composite materials retained their crystallinity and structural integrity during the incorporation of PVA and HA. Furthermore, as the MOF content increased, a clear trend of gradually intensifying U6N characteristic peaks was observed in the XRD patterns.

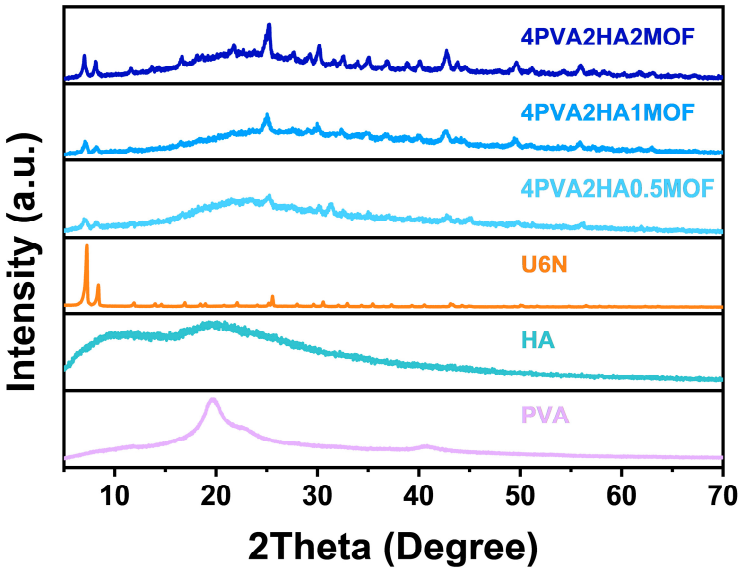


Figure 5. XRD patterns of U6N, HA, PVA and PVA/HA/U6N hydrogels.

3.3. Mechanical Properties Testing of PVA/HA/U6N Hydrogels

The viscoelastic properties of hydrogels significantly influence their mechanical and peelable performance, which in turn determines their effectiveness in surface decontamination processes. To elucidate the rheological properties of the hydrogels, dynamic frequency sweep tests were conducted on 4PVA2HA0.5U6N, 4PVA2HA1U6N, and 4PVA2HA2U6N hydrogels. As shown in Figure 6a, within the angular frequency range of 0.1–10 Hz, the hydrogels exhibited pronounced viscoelastic behavior, characterized by excellent energy storage capacity and deformation recovery properties. Notably, across all tested frequencies, the storage modulus (G′) of the three hydrogels was consistently higher than the loss modulus (G″), indicating dominant elastic behavior. Among them, 4PVA2HA1U6N demonstrated a significantly higher storage modulus compared to the other hydrogels, likely due to its optimal U6N content, which provided sufficient mechanical reinforcement without causing aggregation or compromising material homogeneity and performance.

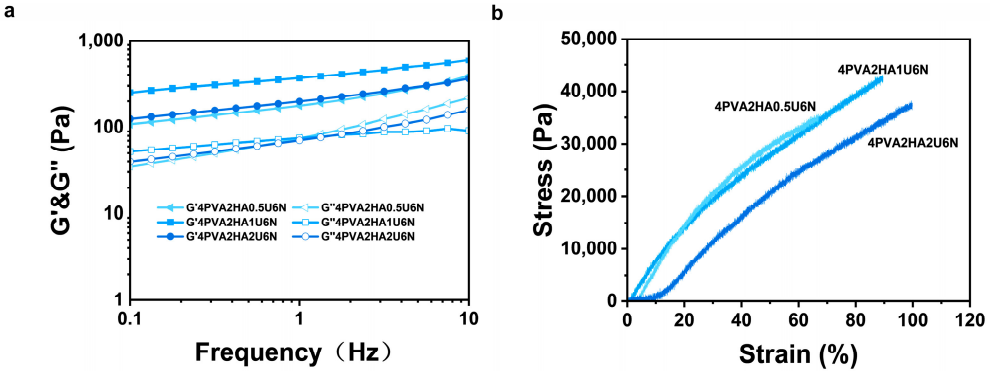


Figure 6. (**a**) Storage modulus and loss modulus plots and (**b**) comparative stress–strain plot obtained by subjecting the synthesized hydrogels to tensile testing.

To further evaluate the mechanical properties of the hydrogels, tensile tests were performed (Figure 6b). The results revealed that these peelable hydrogels, designed for the decontamination of chemical warfare agent simulants, exhibited remarkable elasticity and extensibility due to their unique MOF-crosslinked structure, primarily driven by amide bonds formed between hyaluronic acid and MOF, as well as hydrogen bonding interactions among the hydrogel components. Specifically, compared to the sample with 0.5% U6N content, 4PVA2HA1U6N demonstrated higher tensile strength and stiffness, indicating enhanced resistance to fracture and elastic deformation under tensile stress. In contrast, the 4PVA2HA2U6N sample, with higher U6N content, maintained structural integrity at high strains and exhibited excellent extensibility, but its tensile strength and stiffness were lower than those of 4PVA2HA1U6N. The tensile test results were consistent with the rheological analysis, further confirming that 4PVA2HA1U6N possesses the optimal mechanical properties, likely due to the formation of a denser and more robust three-dimensional network structure within the hydrogel.

3.4. Catalytic Degradation of DMNP by U6N and PVA/HA/U6N Hydrogels

To investigate the catalytic degradation performance of U6N on DMNP and the influence of hydrogels with varying PVA and HA content on the catalytic degradation efficiency, degradation experiments were conducted using U6N and three hydrogels with different mass ratios (PVA:HA:MOF = 8:4:1, 4:2:1, and 2:1:1). During the degradation of DMNP by U6N, the P-O bond in DMNP interacts with the unsaturated sites of Zr-MOF. Hydrogen bonds can form between DMNP and water molecules coordinated to adjacent Zr nodes, while π-π stacking interactions between the aromatic rings of DMNP and the linker molecules in the MOF framework enhance the stability of these hydrogen bonds. Subsequently, in the presence of an alkaline aqueous solution, the generated hydroxyl groups initiate a nucleophilic attack on the organophosphate ester. The coordination of the phosphoryl oxygen atom in DMNP with the Lewis acidic Zr atoms facilitates the hydrolysis of DMNP.

To accurately monitor and analyze the degradation process of DMNP, we conducted UV–Vis spectroscopy tests on the reaction systems, as shown in Figure 7a–d. In Figure 7a, the spectral analysis revealed that when U6N was used as the catalyst, the characteristic absorption peak of DMNP at 275 nm gradually decreased in intensity over time, indicating a reduction in DMNP concentration. Simultaneously, the characteristic absorption peak of 4-NP at 404 nm significantly increased, confirming the effective degradation of DMNP into 4-NP. This trend was consistently observed in the 4PVA2HA0.5U6N, 4PVA2HA1U6N, and 4PVA2HA2U6N hydrogel (Figure 7b–d), further supporting the high efficiency of the catalytic reaction.

To quantify the degradation kinetics, we fitted the experimental data to a pseudo-first-order kinetic model (Figure 8a). The results showed that the half-lives ($t_{1/2}$) for DMNP degradation in the 4PVA2HA0.5U6N, 4PVA2HA1U6N, 4PVA2HA2U6N hydrogels, and U6N were 11.2 min, 10.2 min, 8.7 min, and 7.7 min, respectively, with corresponding rate constants (k) of 0.062 min^{-1}, 0.068 min^{-1}, 0.079 min^{-1}, and 0.089 min^{-1}. Compared to pure U6N, the slightly reduced catalytic efficiency of the hydrogel systems may be attributed to the partial shielding of U6N's active sites by the three-dimensional network within the hydrogels.

Notably, all systems demonstrated excellent degradation performance (Figure 8b). Within 60 min, both U6N and the hydrogel systems achieved over 90% degradation of DMNP. These results indicate that the incorporation of PVA and HA not only imparts superior mechanical properties to the material but also maintains high catalytic degradation efficiency. In summary, through systematic spectroscopic analysis and kinetic studies, this

work validates the potential of U6N-based hydrogels for practical applications. Future studies could focus on optimizing the hydrogel composition to balance catalytic activity and mechanical performance, advancing their application in chemical warfare agent decontamination.

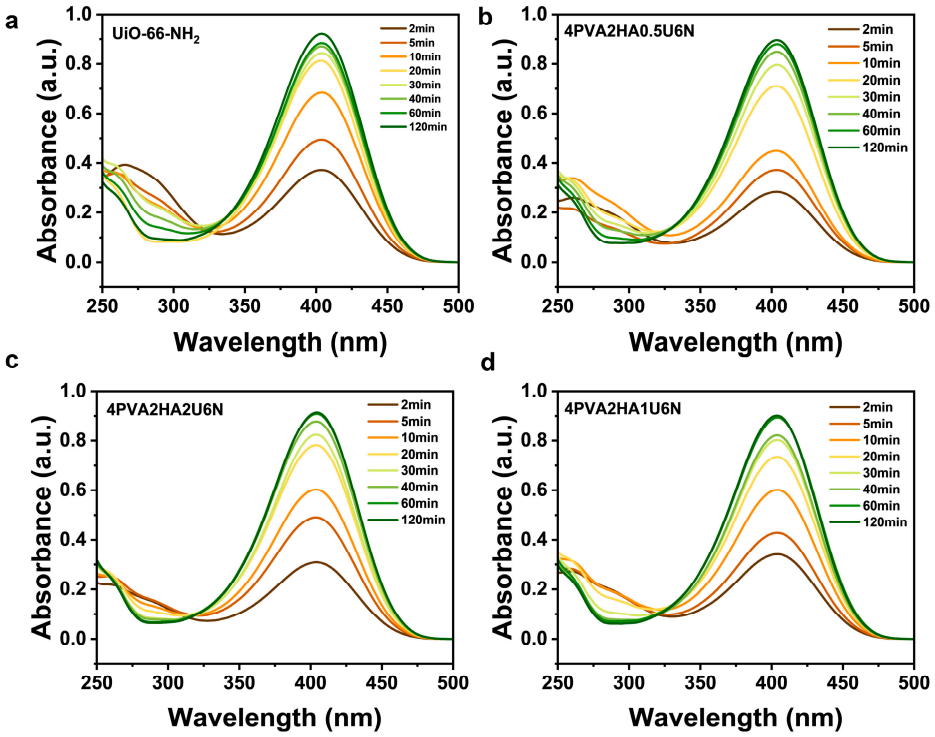


Figure 7. UV–vis spectra of the DMNP hydrolysis with (**a**) U6N, (**b**–**d**) 4PVA2HA0.5U6N, 4PVA2HA1U6N, 4PVA2HA2U6N.

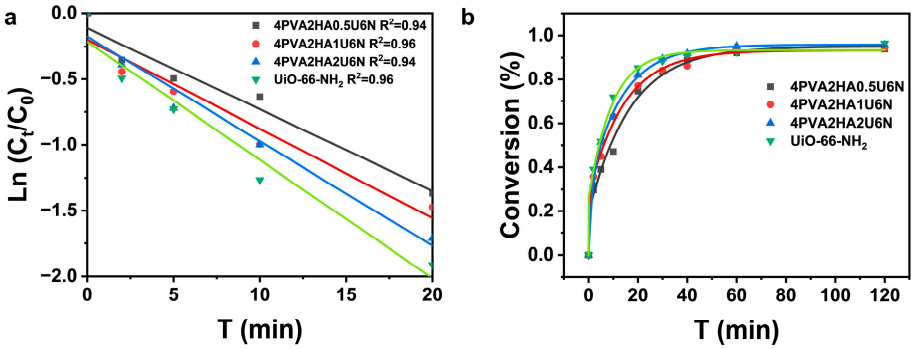


Figure 8. (**a**) Kinetic linear fitting curves of DMNP using U6N, 4PVA2HA0.5U6N, 4PVA2HA1U6N, and 4PVA2HA2U6N and (**b**) the degradation conversion rate of DMNP, 4PVA2HA0.5U6N, 4PVA2HA1U6N, and 4PVA2HA2U6N.

3.5. Adhesive Properties and Peelability of PVA/HA/U6N Hydrogels

To ensure that the hydrogel can adhere tightly and firmly to contaminated substrates, thereby effectively extending the decontamination duration, adhesion experiments were conducted to evaluate the macroscopic adhesive capabilities of the hydrogel. Specifically, the hydrogel was brought into contact with glass and plastic surfaces. The experimental results, as shown in Figure 9, demonstrate that the hydrogel exhibits excellent adhesive properties, firmly adhering to the surfaces of these materials. This strongly indicates that the hydrogel possesses the ability to adhere to contaminated substrates of various materials in practical applications, providing a solid foundation for its effective performance and prolonged decontamination efficacy.

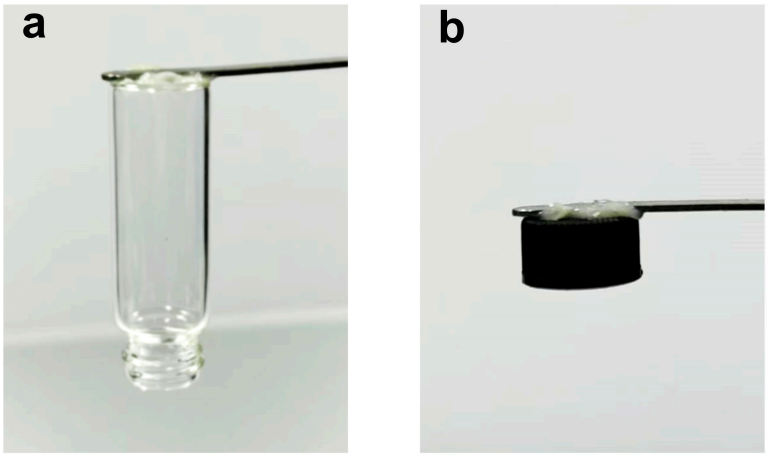


Figure 9. (**a**) The hydrogel adheres to the glass and (**b**) The hydrogel adheres to the plastic.

Considering the practical application scenarios of hydrogels, it is essential to confirm the adhesive performance and peelability of hydrogel films on substrate surfaces. After synthesizing the hydrogel, a portion was applied to common materials such as wood, steel plates, glass, and ceramics. As shown in the Figure 10, the hydrogel effectively adhered to the surfaces of all four materials. After 6 h, the hydrogel remained stable and could be completely peeled off from the surfaces without damaging the substrates. Additionally, due to the non-corrosive nature of the hydrogel components, the substrate surfaces were unaffected after peeling. This characteristic not only demonstrates the excellent adaptability of the hydrogel in practical applications but also provides reliable assurance for its use in a wider range of scenarios.

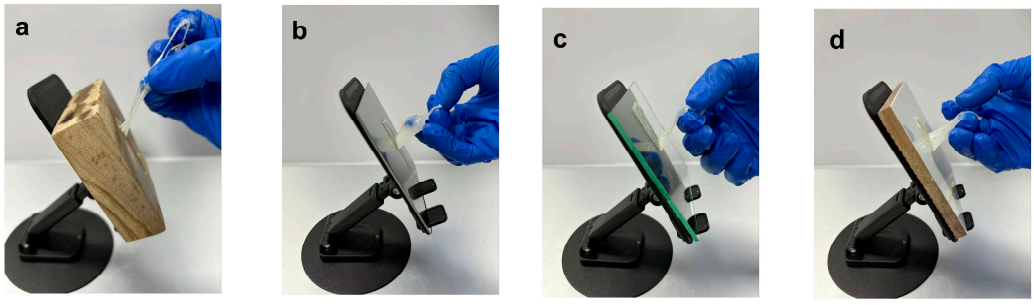


Figure 10. Gel removed from different surfaces after 6 h: (**a**) wood surface, (**b**) metal surface, (**c**) glass surface, (**d**) tile surface.

4. Conclusions

This study developed a kind of U6N-crosslinked nanocomposite hydrogel for efficient degradation of CWA simulants. Through precise modulation of MOF content, the 4PVA2HA1U6N hydrogel with 1.0 wt% U6N exhibited optimal mechanical strength and achieved over 90% degradation efficiency for DMNP within 1 h. Mechanistic investigations revealed that covalent crosslinking between -NH_2 and -COOH groups established a stable three-dimensional network structure, enhancing mechanical robustness and environmental stability through optimized stress distribution via covalent interactions. Post-crosslinking, the hydrogel formed a film morphology, enabling complete post-decontamination peel-off recovery. By integrating MOFs into the hydrogel matrix, this design effectively addresses the technical limitations of traditional powdered MOFs, such as aggregation and poor immobilization, while simultaneously achieving high catalytic efficiency and operational recyclability. The proposed strategy provides an innovative approach for developing

advanced decontamination materials, demonstrating promising potential for chemical warfare agent decontamination and emergency response scenarios.

Author Contributions: Conceptualization, C.W. and G.X.; methodology, S.L.; software, J.Z., Y.L. and M.T.; validation, S.L.; formal analysis, C.W. and S.L.; investigation, S.L.; resources, C.W. and L.W.; data curation, S.L.; writing—original draft preparation, S.L.; writing—review and editing, C.W. and G.X.; visualization, S.L.; supervision, C.W.; project administration, C.W.; funding acquisition, C.W. and L.W. All authors have read and agreed to the published version of the manuscript.

Funding: This research received no external funding.

Data Availability Statement: The data that support the findings of this study are available from the corresponding author upon reasonable request.

Acknowledgments: The authors declare that no acknowledgments are applicable to this work.

Conflicts of Interest: The authors declare no conflicts of interest.

References

1. Chauhan, S.; Chauhan, S.; D'Cruz, R.; Faruqi, S.; Singh, K.K.; Varma, S.; Singh, M.; Karthik, V. Chemical Warfare Agents. *Environ. Toxicol. Pharmacol.* **2008**, *26*, 113–122. [CrossRef] [PubMed]
2. Mangerich, A.; Esser, C. Chemical Warfare in the First World War: Reflections 100 Years Later. *Arch. Toxicol.* **2014**, *88*, 1909–1911. [CrossRef] [PubMed]
3. Zhu, B.; Sheng, R.; Chen, T.; Rodrigues, J.; Song, Q.-H.; Hu, X.; Zeng, L. Molecular Engineered Optical Probes for Chemical Warfare Agents and Their Mimics: Advances, Challenges and Perspectives. *Coord. Chem. Rev.* **2022**, *463*, 214527. [CrossRef]
4. Fuchs, A.; Giuliano, E.A.; Sinha, N.R.; Mohan, R.R. Ocular Toxicity of Mustard Gas: A Concise Review. *Toxicol. Lett.* **2021**, *343*, 21–27. [CrossRef]
5. Szinicz, L.; Worek, F.; Thiermann, H.; Kehe, K.; Eckert, S.; Eyer, P. Development of Antidotes: Problems and Strategies. *Toxicology* **2007**, *233*, 23–30. [CrossRef]
6. Bigley, A.N.; Raushel, F.M. The Evolution of Phosphotriesterase for Decontamination and Detoxification of Organophosphorus Chemical Warfare Agents. *Chem. Biol. Interact.* **2019**, *308*, 80–88. [CrossRef]
7. Bisio, C.; Carniato, F.; Palumbo, C.; Safronyuk, S.L.; Starodub, M.F.; Katsev, A.M.; Marchese, L.; Guidotti, M. Nanosized Inorganic Metal Oxides as Heterogeneous Catalysts for the Degradation of Chemical Warfare Agents. *Catal. Today* **2016**, *277*, 192–199. [CrossRef]
8. Wagner, G.W.; Procell, L.R.; O'Connor, R.J.; Munavalli, S.; Carnes, C.L.; Kapoor, P.N.; Klabunde, K.J. Reactions of VX, GB, GD, and HD with Nanosize Al_2O_3. Formation of Aluminophosphonates. *J. Am. Chem. Soc.* **2001**, *123*, 1636–1644. [CrossRef]
9. Bromberg, L.; Pomerantz, N.; Schreuder-Gibson, H.; Hatton, T.A. Degradation of Chemical Threats by Brominated Polymer Networks. *Ind. Eng. Chem. Res.* **2014**, *53*, 18761–18774. [CrossRef]
10. Bromberg, L.; Schreuder-Gibson, H.; Creasy, W.R.; McGarvey, D.J.; Fry, R.A.; Hatton, T.A. Degradation of Chemical Warfare Agents by Reactive Polymers. *Ind. Eng. Chem. Res.* **2009**, *48*, 1650–1659. [CrossRef]
11. Collins-Wildman, D.L.; Kim, M.; Sullivan, K.P.; Plonka, A.M.; Frenkel, A.I.; Musaev, D.G.; Hill, C.L. Buffer-Induced Acceleration and Inhibition in Polyoxometalate-Catalyzed Organophosphorus Ester Hydrolysis. *ACS Catal.* **2018**, *8*, 7068–7076. [CrossRef]
12. Wagner, G.W.; Peterson, G.W.; Mahle, J.J. Effect of Adsorbed Water and Surface Hydroxyls on the Hydrolysis of VX, GD, and HD on Titania Materials: The Development of Self-Decontaminating Paints. *Ind. Eng. Chem. Res.* **2012**, *51*, 3598–3603. [CrossRef]
13. DeCoste, J.B.; Peterson, G.W. Metal–Organic Frameworks for Air Purification of Toxic Chemicals. *Chem. Rev.* **2014**, *114*, 5695–5727. [CrossRef]
14. Liu, H.; Xu, M.; Li, G.; Zhang, W.; An, T. Solar-Light-Triggered Regenerative Adsorption Removal of Styrene by Silver Nanoparticles Incorporated in Metal–Organic Frameworks. *Environ. Sci. Nano* **2021**, *8*, 543–553. [CrossRef]
15. Ding, X.; Liu, H.; Chen, J.; Wen, M.; Li, G.; An, T.; Zhao, H. *In Situ* Growth of Well-Aligned Ni-MOF Nanosheets on Nickel Foam for Enhanced Photocatalytic Degradation of Typical Volatile Organic Compounds. *Nanoscale* **2020**, *12*, 9462–9470. [CrossRef]
16. Wen, M.; Li, G.; Liu, H.; Chen, J.; An, T.; Yamashita, H. Metal–Organic Framework-Based Nanomaterials for Adsorption and Photocatalytic Degradation of Gaseous Pollutants: Recent Progress and Challenges. *Environ. Sci. Nano* **2019**, *6*, 1006–1025. [CrossRef]
17. Liu, H.; Li, N.; Feng, M.; Li, G.; Zhang, W.; An, T. Near-Infrared Light Induced Adsorption–Desorption Cycle for VOC Recovery by Integration of Metal–Organic Frameworks with Graphene Oxide Nanosheets. *Environ. Sci. Nano* **2022**, *9*, 1858–1868. [CrossRef]

18. Ploskonka, A.M.; DeCoste, J.B. Insight into Organophosphate Chemical Warfare Agent Simulant Hydrolysis in Metal-Organic Frameworks. *J. Hazard. Mater.* **2019**, *375*, 191–197. [CrossRef]
19. Moon, S.; Liu, Y.; Hupp, J.T.; Farha, O.K. Instantaneous Hydrolysis of Nerve-Agent Simulants with a Six-Connected Zirconium-Based Metal–Organic Framework. *Angew. Chem.* **2015**, *127*, 6899–6903. [CrossRef]
20. Shen, A.; Hao, X.; Zhang, L.; Du, M.; Li, M.; Zhao, Y.; Li, Z.; Hou, L.; Duan, R.; Yang, Y. Solid-State Degradation and Visual Detection of the Nerve Agent GB by SA@UiO-66-NH_2@PAMAM Hydrogel. *Polym. Chem.* **2022**, *13*, 6205–6212. [CrossRef]
21. Ma, K.; Wasson, M.C.; Wang, X.; Zhang, X.; Idrees, K.B.; Chen, Z.; Wu, Y.; Lee, S.-J.; Cao, R.; Chen, Y.; et al. Near-Instantaneous Catalytic Hydrolysis of Organophosphorus Nerve Agents with Zirconium-Based MOF/Hydrogel Composites. *Chem Catal.* **2021**, *1*, 721–733. [CrossRef]
22. Wang, X.; Yang, J.; Zhang, M.; Hu, Q.; Li, B.-X.; Qu, J.; Yu, Z.-Z.; Yang, D. Spontaneously Super-Hygroscopic MOF-Gel Microreactors for Efficient Detoxification of Nerve Agent Simulant in Atmospheric Environments. *Appl. Catal. B Environ.* **2023**, *328*, 122516. [CrossRef]
23. Redy Keisar, O.; Nahum, V.; Yehezkel, L.; Marcovitch, I.; Columbus, I.; Fridkin, G.; Chen, R. Active and Strippable PVA/Borax/$NaBO_3$ Hydrogel for Effective Containment and Decontamination of Chemical Warfare Agents. *ACS Omega* **2021**, *6*, 5359–5367. [CrossRef] [PubMed]
24. Toader, G.; Ginghina, R.-E.; Bratu, A.E.; Podaru, A.I.; Pulpea, D.; Rotariu, T.; Gavrilă, A.M.; Diacon, A. Ionic Crosslinked Hydrogel Films for Immediate Decontamination of Chemical Warfare Agents. *Gels* **2024**, *10*, 428. [CrossRef]
25. Hu, Q.; Wang, X.; Zheng, Y.; Zhao, T.; Qu, J.; Yu, Z.-Z.; Yang, D. Solar-Thermally Enhanced Catalytic Hydrolysis of Chemical Warfare Agent Simulant with UiO-66-NCS Decorated Reduced Graphene Oxide Aerogels. *Chem. Eng. J.* **2023**, *476*, 146606. [CrossRef]
26. Zhang, M.; Sun, Q.; Wang, Y.; Shan, W.; Lou, Z.; Xiong, Y. Synthesis of Porous UiO-66-NH_2-Based Mixed Matrix Membranes with High Stability, Flux and Separation Selectivity for Ga(III). *Chem. Eng. J.* **2021**, *421*, 129748. [CrossRef]
27. Zhang, X.; Liu, M.; Han, R. Adsorption of Phosphate on UiO-66-NH_2 Prepared by a Green Synthesis Method. *J. Environ. Chem. Eng.* **2021**, *9*, 106672. [CrossRef]
28. Heu, R.; Ateia, M.; Awfa, D.; Punyapalakul, P.; Yoshimura, C. Photocatalytic Degradation of Organic Micropollutants in Water by Zr-MOF/GO Composites. *J. Compos. Sci.* **2020**, *4*, 54. [CrossRef]
29. Lin, K.-Y.A.; Liu, Y.-T.; Chen, S.-Y. Adsorption of Fluoride to UiO-66-NH_2 in Water: Stability, Kinetic, Isotherm and Thermodynamic Studies. *J. Colloid Interface Sci.* **2016**, *461*, 79–87. [CrossRef]
30. Zhao, F.; Yang, W.; Han, Y.; Luo, X.; Tang, W.; Yue, T.; Li, Z. A Straightforward Strategy to Synthesize Supramolecular Amorphous Zirconium Metal-Organic Gel for Efficient Pb(II) Removal. *Chem. Eng. J.* **2021**, *407*, 126744. [CrossRef]
31. Fang, L.; Wu, B.; Lo, I.M.C. Fabrication of Silica-Free Superparamagnetic ZrO_2@Fe_3O_4 with Enhanced Phosphate Recovery from Sewage: Performance and Adsorption Mechanism. *Chem. Eng. J.* **2017**, *319*, 258–267. [CrossRef]
32. Soylu, P.; Başlak, C.; Kılıçoğlu, P.; Kula, İ.H.; Koçer, M.B.; Albayatı, S.H.M. A Simple UiO-66-NH_2@MWCNTs-COOH Based Electrochemical Sensor for the Sensitive Detection of Tert-Butylhydroquinone in Edible Oils. *Microchem. J.* **2024**, *205*, 111331. [CrossRef]
33. Wang, Y.; Zhao, W.; Qi, Z.; Zhang, L.; Zhang, Y.; Huang, H.; Peng, Y. Designing ZIF-8/Hydroxylated MWCNT Nanocomposites for Phosphate Adsorption from Water: Capability and Mechanism. *Chem. Eng. J.* **2020**, *394*, 124992. [CrossRef]

Disclaimer/Publisher's Note: The statements, opinions and data contained in all publications are solely those of the individual author(s) and contributor(s) and not of MDPI and/or the editor(s). MDPI and/or the editor(s) disclaim responsibility for any injury to people or property resulting from any ideas, methods, instructions or products referred to in the content.